

Hybrid Approach for Enhancing Lesion Segmentation in Fundus Images

Mohammadmahdi Eshragh, Emad A. Mohammed, Behrouz Far, Ezekiel Weis, Carol L Shields, Sandor R Ferenczy, and Trafford Crump

Abstract—Choroidal nevi are common benign pigmented lesions in the eye, with a small risk of transforming into melanoma. Early detection is critical to improving survival rates, but misdiagnosis or delayed diagnosis can lead to poor outcomes. Despite advancements in AI-based image analysis, diagnosing choroidal nevi in colour fundus images remains challenging, particularly for clinicians without specialized expertise. Existing datasets often suffer from low resolution and inconsistent labelling, limiting the effectiveness of segmentation models. This paper addresses the challenge of achieving precise segmentation of fundus lesions, a critical step toward developing robust diagnostic tools. While deep learning models like U-Net have demonstrated effectiveness, their accuracy heavily depends on the quality and quantity of annotated data. Previous mathematical/clustering segmentation methods, though accurate, required extensive human input, making them impractical for medical applications. This paper proposes a novel approach that combines mathematical/clustering segmentation models with insights from U-Net, leveraging the strengths of both methods. This hybrid model improves accuracy, reduces the need for large-scale training data, and achieves significant performance gains on high-resolution fundus images. The proposed model achieves a Dice coefficient of 89.7% and an IoU of 80.01% on 1024×1024 fundus images, outperforming the Attention U-Net model, which achieved 51.3% and 34.2%, respectively. It also demonstrated better generalizability on external datasets. This work forms a part of a broader effort to develop a decision support system for choroidal nevus diagnosis, with potential applications in automated lesion annotation to enhance the speed and accuracy of diagnosis and monitoring.

This research is funded by New Frontiers Research Fund - Explorations grant

Submission Date: February 20 2025

Mohammadmahdi Eshragh is with Department of Electrical & Software Engineering, University of Calgary, Canada. (Email: Mohammadmahdi.eshragh@ucalgary.ca)

Emad A. Mohammed is with the Department of Computer Science and Physics, Wilfrid Laurier University, Waterloo, Canada. (Email: emohammed@wlu.ca)

Behrouz Far is with Department of Electrical & Software Engineering, University of Calgary, Canada. (Email: Far@ucalgary.ca)

Ezekiel Weis is with Dept of Ophthalmology & Visual Sciences, University of Alberta, Edmonton, Canada. (Email: Ezekiel@ualberta.ca)

Carol L. Shields is with the Wills Eye Hospital, Philadelphia, USA. (Email: carol.shields@shieldsoncology.com)

Sandor R. Ferenczy is with the Wills Eye Hospital, Philadelphia, USA. (Email: sandor@shields.md)

Trafford Crump is with the Department of Surgery, University of Calgary, Canada. (Email: Tcrump@ucalgary.ca)

Index Terms—Image Segmentation, Choroidal Nevi, Convolutional Neural Networks, U-Net, Lesion Segmentation.

I. INTRODUCTION

Medical image diagnostics, particularly in identifying abnormalities such as cancer, are both challenging and time-consuming [1], [2]. These challenges arise from the need to analyze complex, high-dimensional data and the reliance on specialist expertise for accurate interpretation. Additionally, diagnostic outcomes can vary due to differences in imaging quality, patient-specific factors, and the inherent subjectivity of manual assessments. Most of the reviewed studies rely on small to medium-sized datasets, often of poor quality, with issues such as low resolution and inconsistent labeling [3]. Collaborative efforts to develop diverse, standardized datasets of diagnostic images are essential to improve diagnostic tools and ensure equitable outcomes [4]. Machine Learning (ML) methods show promise in enhancing accuracy and speed in identifying abnormalities in medical images because of their ability to automatically learn and extract complex patterns and features from large datasets, reducing reliance on manual interpretation, and their capacity to generalize across diverse cases, enabling efficient and consistent diagnostic support. Such is the case when identifying choroidal nevi (CN), commonly characterized as a lesion in the back of the eye, in fundus images. Fundus images shown in Fig4 are diagnostic photographs of the eye's interior surface, capturing detailed views of the retina, optic nerve head, macula, retinal blood vessels, and choroid [5]. Fundus images are crucial for detecting and monitoring ophthalmic conditions such as CN, choroidal melanoma (CM), diabetic retinopathy, age-related macular degeneration, and glaucoma. It is important to identify CN because a small percentage of it will be malignant in the form of CM, occurring in about 6 out of 1 million person-years [4], [6]. If not detected early enough, CM can result in vision loss, metastasis, or death [7]. Segmenting CN in fundus images poses a significant challenge for machine learning because of many challenges, like indistinct boundaries and fading colour spectra or the scarcity of annotated datasets. To address these challenges, this paper introduces and evaluates an innovative approach that combines convolutional neural network (CNN) models with mathematical/clustering (traditional) segmentation methods for automated fundus image segmentation. This

combined approach is intended to overcome the technical obstacles, ultimately advancing the precision and reliability of CN lesion segmentation. This research is part of a larger project to develop a decision support system for CN diagnosis, focusing on creating a segmentation algorithm to identify key areas in colour fundus images [2], [8]–[12].

II. OBJECTIVES

A. Addressing Lesion Border Uncertainty:

The primary challenge in this research lies in the ambiguity of segmentation CN lesion borders in model-generated masks of fundus images. Lesions in images lack clear borders, blending into surrounding areas with colour gradations, complicating accurate boundary definition [2] (Fig. 6). Additionally, manual delineation of lesion borders for mask creation is challenging even for eye care professionals due to the ambiguous nature of lesion boundaries [13]. When used for model training, these minor inaccuracies in manually created masks can lead to amplified errors in the model's ability to differentiate lesions from the background, reflecting the initial uncertainties in manual mask creation.

B. Reducing Dataset Dependency

Another challenge is that most ML models require large and high-quality annotated data sets, which are scarce in the medical domain due to the labour-intensive nature of annotation [14]. As illustrated in Table III, there is currently no publicly available annotated dataset for CN segmentation, and the private datasets are not large enough.

C. Improving accuracy when training with original-size images:

The results of experiment 1 in this research are presented in Table I and demonstrate improvement in training a U-net model when the image size is reduced. This paper identifies three primary factors contributing to this phenomenon.

Measurements	Image Size			
	128*128	256*256	512*512	1024*1024
IoU	74.82%	66.77%	46.44%	34.20%
Dice	84.32%	79.70%	62.43%	51.30%

TABLE I: Experiment 1 - Training the U-net with different image sizes

Firstly, signal-to-noise ratio: in this study, the "signal" is the actual CN/CM lesion area in the eye fundus images, while noise can come from the background and various sources such as imaging artifacts (e.g., an eyelash) or unwanted variations in pixel intensity (e.g. "camera flare" or flash). When the image size is reduced, the noise diminishes more than the signal. This is because the distinction between the lesion and the rest of the image remains clear while much of the irrelevant data is

eliminated. Based on the previous study [13] which used the same dataset, it is known that the lesions on average, occupy less than 2 percent of the entire fundus image dataset.

Secondly, noise distribution: when working with smaller images, the noise is more evenly distributed, allowing the network to focus more effectively on relevant features without being overwhelmed by the noise present in larger images [15]. **Thirdly**, network capacity: the capacity of U-Net is limited, which means this network is not designed for large-size images, and while the network can be made deeper, the gradient diminishing problem must be considered [16]–[18]. This research addresses this challenge by employing an alternative image segmentation method that is less noise-sensitive. This approach enables the development of original large-size image segmentation models without compromising accuracy, as observed with U-Net models.

D. Training Time and Energy Usage on Large-Size Images

Based on experiment 1 (Table I), training a U-Net model on original large-size images is time-consuming and energy-intensive without yielding a corresponding increase in accuracy. Conversely, training a U-Net on smaller images is faster, more energy-efficient, and results in higher accuracy (Table II). Leveraging these results, we developed a Hybrid segmentation model capable of making predictions on large-size images without requiring training on large-size images. This approach results in better outcomes with reduced time and energy consumption.

Measurements	Image Size			
	128*128	256*256	512*512	1024*1024
Training Time (Min)	3.16	11.20	37.00	129.30
Energy Usage (Wh)	15.8	56	185	646.5

TABLE II: Experiment 1 - Training time and energy consumption for different image sizes.

E. Addressing Generalizability:

One of the significant challenges U-Net models face is the decline in accuracy when the raw data for prediction originates from a different domain, such as images captured by different fundus cameras [19]. The accuracy drops notably in such cases, although the model still manages to predict most lesion areas. In machine learning, domain adaptation can address this problem, but the model must be retrained on a new dataset from the new domain. However, the method proposed in this study is not dependent on the dataset. It performs clustering segmentation based on the image's colours and various visual aspects, making it less susceptible to the domain shift issues that purely machine learning-based models encounter.

III. RELATED WORKS

A. Literature Review

Neubert *et al.* presented Compact Watershed and Preemptive SLIC: On improving trade-offs of superpixel segmentation algorithms. This paper contributed to the field by introducing two new adaptations of superpixel segmentation algorithms that balanced key trade-offs between segmentation quality, stability, and runtime. Their experimental results provided detailed insights into the effects of the proposed algorithmic changes. Additionally, they offered open-source implementations of Preemptive SLIC and the enhanced Seeded Watershed algorithm, facilitating further research and practical applications [20]. By addressing the computational efficiency of SLIC and improving the regularity of watershed segments, their work expanded the boundaries of real-time superpixel segmentation and enhanced its applicability in various domains.

Felzenszwalb *et al.* introduced an efficient image segmentation algorithm based on graph theory, which aimed to capture perceptually important regions while maintaining computational speed. Unlike traditional methods, it adapted its segmentation criteria based on the variability of neighbouring regions, ensuring detail preservation in low-variability areas and effective segmentation in high-variability regions. The approach ran nearly linearly relative to image size, making it practical for real-time applications like video processing and large-scale image databases [21].

Achanta *et al.* empirically evaluated five state-of-the-art superpixel algorithms concerning boundary adherence, speed, memory efficiency, and segmentation performance [22]. They introduced the simple linear iterative clustering (SLIC) algorithm, which adapted k-means clustering, and found that SLIC matched or exceeded previous methods in boundary adherence. Furthermore, SLIC demonstrated superior speed and memory efficiency while enhancing segmentation accuracy, highlighting its versatility for superpixel generation.

Jiang *et al.* developed a novel multi-path recurrent U-Net for retinal fundus image segmentation, which demonstrated efficacy in segmenting retinal vessels and optic structures [23]. On the Drishti-GS1 dataset [24], the model achieved Dice scores of 98.17% for optic disc segmentation and 89.21% for optic cup segmentation.

Alom *et al.* introduced R2U-Net, novel architectures for medical image segmentation that integrated elements of U-Net, residual networks, and recurrent CNNs [17], [18]. They focused on enhancing segmentation precision in areas such as retinal images, skin cancer, and lung diseases. Their paper demonstrated the superiority of these models over existing ones on multiple benchmark datasets, highlighting their applicability in diverse medical imaging contexts.

Zhao *et al.* proposed an attention U-Net with pre-trained models for OCS and ODS [25]. The modified architecture included eleven convolutional layers with max-pooling layers in the encoding path and five deconvolution layers in the decoding path. They created an attention gate for each skip connection in the network to maintain positive characteristics and spatial data. The model achieved an accuracy of 99.75% on the DRISHTI-GS dataset.

Shirokanev *et al.* explored fundus image segmentation using CNNs, focusing on four image classes: healthy areas, exudates, and thick and thin blood vessels [26]. They employed the HSL colour model and identified the H channel as the most informative for feature extraction, with a 7% segmentation error for exudates. Additionally, they assessed the resilience of CNNs to different noises, revealing sensitivity to impulse noise and instability with Gaussian white noise.

Li *et al.* enhanced UNet++ with a residual unit and attention mechanism, which improved segmentation accuracy [27]. They tested the modified model on skin cancer, cell nuclei, and angiography datasets. The model demonstrated high scores, achieving 82.32% IoU and 88.59% Dice for skin cancer, 85.91% Dice and 87.74% IoU for cell nuclei, and 72.48% Dice with 66.57% IoU for angiography.

Mubashar *et al.* proposed R2U++, a U-Net-based architecture for medical image segmentation [28]. It featured deep recurrent residual blocks and dense skip pathways, which improved feature extraction and segmentation. They tested R2U++ across various modalities, including electron microscopy, X-rays, fundus imaging, and CT scans, and it demonstrated notable improvements over UNet++ and R2U-Net in IoU and Dice scores. The review covered various algorithms and architectures for medical image segmentation, focusing on fundus images. It discussed multi-path recurrent U-Net, Residual U-Net, attention U-Net, and R2U++, evaluating their effectiveness across different datasets to highlight their applicability in medical imaging. Specialized algorithms were identified as necessary for segmenting choroidal nevi since existing medical image segmentation methods, which focused on areas like retinal vessels and optic structures, did not address its unique features. This highlighted the need to develop specific algorithms for effective choroidal nevi segmentation, which is crucial for accurate diagnosis and treatment.

Biglarbeiki *et al.* [29] utilized the YOLOv8 segmentation model to improve choroidal nevi segmentation in fundus images. They combined patch-based and full-size image training, data augmentation, and post-processing to address challenges such as limited data and class imbalance. Their approach achieved Dice scores of 0.833 and 0.764 across datasets. This work demonstrated the potential of YOLOv8 for accurate segmentation, reducing reliance on manual methods and enabling timely detection of malignant transformations.

B. Research Gap and Motivation

Accurate segmentation of CN lesions in fundus images remains a significant challenge due to their indistinct borders, sensitivity to noise, and the requirement for large, high-quality annotated datasets. Existing methods, including deep learning models like U-Net, often face challenges in accurately segmenting the lesion borders, particularly for large images or images from varied sources. Manual delineation of these lesions is not only labor intensive, but also prone to inaccuracies, even when performed by experts. These limitations lead to unreliable training data and hinder the development of generalized models. Additionally, traditional segmentation methods,

while effective in some scenarios, require laborious manual parameter selection, making them impractical for broader applications. The need for a method that addresses these gaps, particularly one that is resource-efficient and performs well on high-resolution images, is paramount for improving early detection and management of CN lesions.

Ref#	Method	Segmented Part	Dataset
[13]	Ensemble U-Net	Choroidal nevi	Private
[29]	Application (YOLO)	Choroidal nevi	Private
[23]	Multi-Path Recurrent U-Net	Vessels & Optic	DRIVE [30]
[25]	U-net & Transfer Learning	Disk & Cup	Drishti-GS [24]

TABLE III: Studies on Fundus image segmentation

C. Contributions

The contributions of this paper, aimed at addressing the identified research gaps, are as follows.

1) Development of a hybrid model: A novel hybrid approach that integrates traditional segmentation techniques with insights derived from the U-Net. This model improves segmentation accuracy, reduces dependency on large-scale training datasets, and enhances generalizability across different image sources.

2) Automated parameter selection: Introduction of an automated parameter selection mechanism for traditional segmentation methods. Traditional segmentation models, such as SLIC, perform segmentation by clustering pixels based on their colour and intensity. As these methods do not require training datasets, they are independent of dataset size, source, and image dimensions. By training a machine learning model on a dataset of smaller images, the method generates data for traditional models, effectively automating the process and reducing the reliance on manual adjustments.

3) Resource-efficient segmentation: A segmentation method capable of achieving high accuracy on high-resolution images without requiring powerful GPUs for inference, enabling practical real-world applications.

These contributions collectively address the challenges of lesion border uncertainty, domain shift sensitivity, and computational inefficiency in existing methods. They provide a significant step forward in the segmentation of CN lesions, offering both theoretical advances and practical solutions for medical image segmentation.

D. Comparison to Previous Research:

In comparison, in the previous paper from this lab [13], the best results achieved were an IoU of 78.09% and a Dice coefficient of 87.70%. That study employed three models (U-Net, Attention U-Net, and Residual U-Net) and utilized an ensemble learning approach to obtain the reported results. Another study [29] achieved Dice coefficients of 83.3% and 76.4% across datasets using a segmentation model to enhance CN segmentation in fundus images. This highlights the potential of YOLOv8 for precise and reliable segmentation. Table III presents a comparison of the most relevant studies on fundus imaging.

IV. DATASET:

A. Dataset Description

This research employs two distinct datasets of images:

1) Original eye fundus images: The Alberta Ocular Brachytherapy Program, based out of Edmonton, Canada, provided a dataset containing 253 anonymized RGB fundus images, offering a detailed representation of various ocular conditions. The original images were 3900x3900 pixels. For the experiments and comparisons, we also created resized versions of these images with dimensions of 128x128, 256x256, 512x512, and 1024x1024 pixels.

2) Ground-Truth Masks for Lesion Identification: Masks of the region of interest were expertly created using ophthalmological expertise and specialized annotation software. Every fundus image was manually annotated to produce a binary mask, using a black-and-white scheme (0 for black, 1 for white) for clear differentiation.

B. Data Preparation Pipeline

Data Normalization Technique in Image Preparation:

Data preparation involved normalizing image pixels, originally 0-255, divided by 256, rescaling them to a 0-1 range for uniformity. The binary masks were inherently within this range, requiring no further adjustment.

V. METHODS

A. Ethical Approval

The datasets used for this study was acquired under a study protocol approved by The Health Research Ethics Board of Alberta Cancer Committee, ID 'HREBA.CC-17-0625. This includes both datasets used in this research.

B. Image Processing:

Superpixels have emerged as a fundamental concept in computer vision and image processing, serving as an intermediary representation between the raw pixel data and the higher-level features used in various algorithms. Here, we delve into definitions, advantages, and applications of superpixels.

Superpixel Definition: A superpixel is a group of adjacent pixels that share common characteristics, such as colour or intensity. Unlike individual pixels, which provide very localized and often noisy information, superpixels aggregate this information into more meaningful and larger entities. This aggregation helps reduce image data complexity while preserving important structural information.

The following four techniques are widely recognized as traditional, low-level methods for image segmentation. Due to the inherent challenges in achieving high-quality segmentations and the subjective nature of defining "good" segmentation based on specific applications, these methods are typically employed to generate over-segmentations, also known as superpixels. These superpixels provide a foundational structure for more advanced algorithms, such as conditional random fields (CRF) [31].

1) Felzenszwalb's efficient graph-based segmentation [21]:

Algorithm Overview Felzenszwalb's graph-based segmentation algorithm operates by representing the image as a graph $G = (V, E)$, where each pixel corresponds to a node $v \in V$ and edges $e \in E$ connect adjacent pixels. The edges are weighted based on the dissimilarity between connected pixels, often using colour or intensity differences.

2) Quickshift image segmentation [32]: Quickshift image segmentation clusters pixels based on colour and spatial proximity using a mode-seeking algorithm. It operates by shifting each pixel towards the mode of its local region iteratively, forming regions that reflect natural boundaries in the image. This method is known for its speed and ability to handle varying segment sizes.

3) SLIC - K-Means based image segmentation [22]: SLIC (Simple Linear Iterative Clustering) segments images by clustering pixels based on colour and spatial information using a K-means approach. It initializes cluster centers on a grid and refines them iteratively, resulting in compact and uniform superpixels. This method balances computational efficiency with high-quality segmentation.

4) Compact watershed segmentation of gradient images [20]:

Compact watershed segmentation enhances traditional watershed methods by incorporating a compactness constraint to produce more coherent and less fragmented segments. This approach uses gradient images to identify boundaries and applies markers to guide segmentation. The compactness constraint penalizes irregular or overly fragmented regions, resulting in more accurate and meaningful segmentation outcomes.

C. Simple Linear Iterative Clustering (SLIC):

Distance Measure, the SLIC algorithm computes the distance between a pixel and a superpixel center using a combination of colour and spatial distances [22]. The distance in CIELAB (International Commission on Illumination) colour space is given by:

$$d_{\text{lab}} = \sqrt{(l_k - l_i)^2 + (a_k - a_i)^2 + (b_k - b_i)^2} \quad (1)$$

where l_k, a_k, b_k are the CIELAB colour components of the superpixel center, and l_i, a_i, b_i are the pixel's colour components.

The spatial distance in the image plane is computed as:

$$d_{\text{xy}} = \sqrt{(x_k - x_i)^2 + (y_k - y_i)^2} \quad (2)$$

where x_k, y_k are the coordinates of the superpixel center, and x_i, y_i are the coordinates of the pixel.

The combined distance measure used to assign pixels to superpixels is:

$$D_s = d_{\text{lab}} + \frac{m}{S} d_{\text{xy}} \quad (3)$$

Here, m controls the compactness of the superpixels, and S is the grid interval, computed as:

$$S = \sqrt{\frac{N}{K}} \quad (4)$$

where N is the total number of pixels in the image, and K is the desired number of superpixels.

D. SLIC Algorithm

The steps of the SLIC algorithm are as follows:

1) Initialize Cluster Centers: The image is divided into a grid of approximately equal-sized superpixels, and the initial cluster centers C_k are chosen at regular grid intervals S , where the cluster centers are initialized as:

$$C_k = [l_k, a_k, b_k, x_k, y_k]^T \quad (5)$$

where l_k, a_k, b_k are the CIELAB colour components, and x_k, y_k are the spatial coordinates of the superpixel center. By applying the transpose (denoted as T), this row vector is converted into a column vector \mathbf{v}^T , where \mathbf{v} is the original row vector. This column vector is more suitable for matrix operations in many linear algebra contexts, such as when performing calculations like averaging the values of the pixels in a superpixel cluster.

2) Perturb Cluster Centers: Each cluster center is moved to the pixel in its neighbourhood with the lowest gradient.

Horizontal Gradient:

$$\|\mathbf{I}(x+1, y) - \mathbf{I}(x-1, y)\|^2 \quad (6)$$

This term measures the change in intensity (I) between two neighbouring pixels along the x-axis at positions $(x+1, y)$ and $(x-1, y)$. The difference represents the horizontal gradient, and squaring it ensures a positive value and emphasizes larger differences.

Vertical Gradient:

$$\|\mathbf{I}(x, y+1) - \mathbf{I}(x, y-1)\|^2 \quad (7)$$

This term calculates the change in intensity between two neighbouring pixels along the y-axis at positions $(x, y+1)$ and $(x, y-1)$. The difference gives the vertical gradient, and squaring it serves the same purpose as the horizontal gradient.

Gradient Magnitude:

$$G(x, y) = \text{HorizontalGradient} + \text{VerticalGradient} \quad (8)$$

The total gradient magnitude is the sum of the squared horizontal and vertical gradients. This represents the overall strength of the gradient at point (x, y) , indicating how much the pixel intensity is changing in the local neighbourhood.

3) Assign Pixels: Each pixel in the image is assigned to the nearest cluster center C_k within a $2S \times 2S$ search area based on the distance measure D_s explained in Eq.3.

4) *Update Cluster Centers*: After assigning pixels to clusters, the cluster centers are recomputed by averaging the colour and spatial coordinates of the pixels belonging to each cluster:

$$C_k = \frac{1}{n_k} \sum_{i \in k} \mathbf{I}(i) \quad (9)$$

5) *Iterate Until Convergence*: The assignment and update steps are repeated until the residual error E , defined as the L1 norm between the previous and new cluster centers, falls below a threshold:

$$E = \sum_k \|C_k^{\text{new}} - C_k^{\text{old}}\| \quad (10)$$

6) *Enforce Connectivity*: Any stray pixels not connected to their assigned superpixel are relabeled with the nearest large superpixel's label.

E. Machine Learning Models

The paper involved training U-net models to detect lesions in fundus images.

1) *Standard U-net Architecture [16]*: The U-net architecture, with its U-shape, merges down-sampling and up-sampling pathways. It uses convolutions, ReLU activations, and max pooling to enhance features while reducing dimensions. Up-sampling combines these features with high-resolution data from the down-sampling path. U-net's success in medical image segmentation led to its use in this study.

2) *Attention U-net Architecture [33]*: The Attention U-net, an evolution of the basic U-net, includes an attention gate mechanism to focus on essential regions and suppress less relevant features. Its lightweight design improves data representation without significantly increasing computational load or model parameters. Its versatility and modular design make it easily integrated into various CNN architectures, enhancing its utility in image analysis.

F. New architecture - a combination of the legacy and modern segmentation methods:

This paper proposes a novel architecture that integrates traditional image segmentation models with contemporary machine learning (ML) techniques, each with distinct strengths and limitations. Traditional segmentation models [20]–[22], [32] often depend on object characteristics such as colour or intensity patterns, requiring manual adjustment of parameters like compactness, the number of segments, and the size of each image's Gaussian kernel (sigma). In contrast, machine learning (ML) models can perform segmentation automatically without user input. However, these models are computationally intensive and require advanced GPUs, especially when training on full-size images. Our approach involves training an ML model on smaller images and then using it to generate the necessary data for the traditional models, thereby automating their operation. The architecture is shown in Fig. 1. This proposed hybrid method addresses several challenges outlined in this paper, including improved segmentation accuracy for larger images, enhanced energy and time efficiency, and better generalizability.

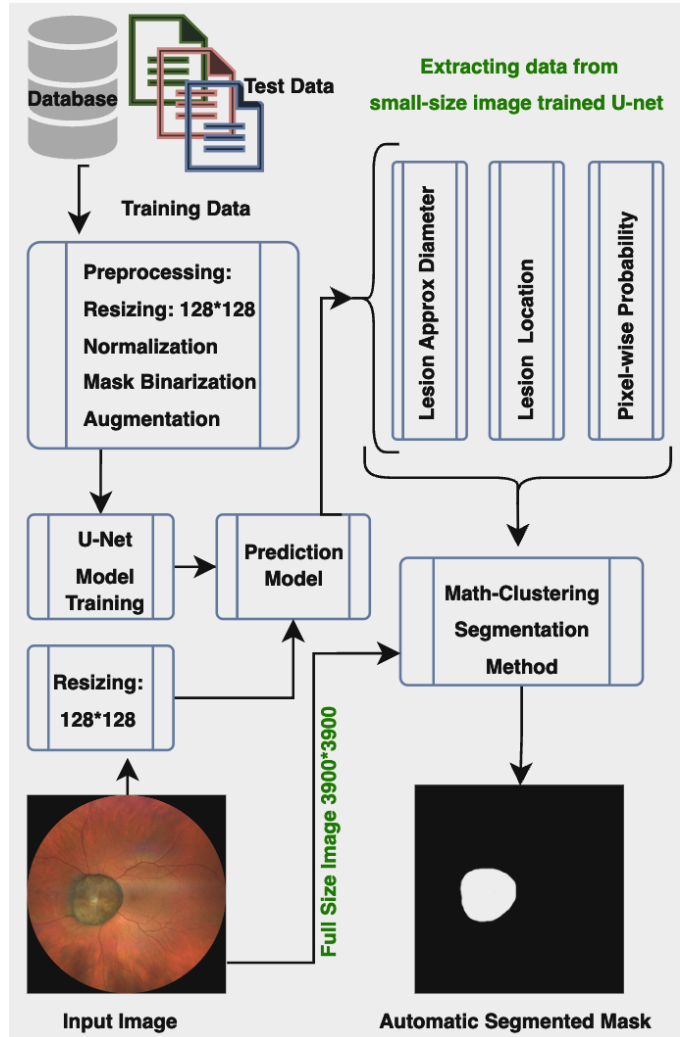


Fig. 1: Proposed Architecture Diagram

1) *Training Attention U-Net on Different Image Sizes*: In this study, Attention U-Net models were trained on images of varying sizes (128x128, 256x256, 512x512, and 1024x1024 pixels) to evaluate their accuracy. To ensure that the results were attributable solely to the performance of the U-Net model, no data augmentation or image cropping was applied. Seed numbers were kept consistent across all stages to prevent variability due to data batching. The data was split into training and testing sets at a ratio of 90/10 percent. Subsequently, the training data was further divided into training and validation subsets at an 80/20 percent ratio. The learning rates were set to 1×10^{-4} for image sizes 128x128 and 256x256, and 1×10^{-5} for image sizes 512x512 and 1024x1024. The models trained on image sizes 128x128 (small-size model) and 1024x1024 (large-size model) pixels were saved for subsequent experiments and comparisons.

2) *Data Extraction from U-Net*: A critical aspect of this method is extracting the necessary information from the "test image" processed by the small-sized model. Specifically, one image from the test set (I_{th}) is selected and processed through the small-sized trained model. The result is a mask that highlights the lesion in the corresponding location of the (I_{th})

fundus image from the test set. This 128x128 pixel mask (I_{th}) is also saved for later use in the data extraction stage. The same (I_{th}) image from the larger dataset (1024x1024 pixels) is then selected and processed through the large-sized model. The accuracy of the segmentation results, measured by the Intersection over Union (IoU) and Dice coefficient, is recorded for both models.

G. Approximate Diameter (Image-to-Lesion Ratio Extraction Function) :

In this study, we developed an image-to-lesion ratio extraction function. This function analyzes the mask and calculates the ratio between the lesion area and the background. By doing so, it provides a **"number of the segments"** (NS) factor for the SLIC function. To calculate the ratio between the total area of the image and the largest connected lesion component in a binary image, the following formula is used:

$$\text{Ratio} = \left(\frac{A_{\text{total}}}{A_{\text{lesion}}} \right) \times C \quad (11)$$

where:

- A_{total} is the total area of the binary image, calculated as:

$$A_{\text{total}} = \text{height} \times \text{width} \quad (12)$$

- A_{lesion} is the area of the largest connected component (lesion) in the binary image.
- C is a calibration factor.

The calculated ratio is then rounded to the closest multiple of 5:

$$\text{Image-to-Lesion Ratio} = \text{round} \left(\frac{\text{Ratio}}{5} \right) \times 5 \quad (13)$$

The calculated ratio is rounded to the nearest multiple of 5, based on the image size, to the largest lesion ratio. If no lesions are detected, a default value of 700 is assigned, representing the image size to the smallest lesion ratio. These values define the image-to-lesion ratio range.

H. Pixel-Wise Probability:

A common issue with traditional computer vision models like SLIC is their lack of intelligence; even if they segment an image accurately, they cannot prioritize or highlight important segments due to the absence of contextual understanding. In this study, we developed a function to address this limitation. This function examines all superpixels and calculates their relevance by comparing them to the lesion identified by the small-sized trained U-Net model. This allows for the selection of the most relevant superpixel to highlight the lesion segment accurately. This section describes extracting superpixels from an image and selecting the most probable superpixel based on the U-Net training results.

Let I represent the input image and S the binary segmentation result from U-Net. The superpixel segmentation is performed using the SLIC algorithm. The steps are outlined below:

1) Superpixel Segmentation: The input image I is segmented into superpixels using the SLIC algorithm, which divides the image into N_{segments} superpixels based on a compactness constraint:

$$\text{superpixels} = \text{SLIC}(I, N_{\text{segments}}, \text{compactness}, \sigma) \quad (14)$$

where:

- N_{segments} is the number of superpixels, defined by the ratio obtained from Eq. 13.
- compactness is the balancing factor between color proximity and spatial proximity.
- σ is the Gaussian smoothing applied before clustering.

2) Resizing the Binary Segmentation: The U-Net model output binary mask S is resized from (128*128) to match the dimensions of the original image:

$$S_{\text{resized}} = \text{Resize}(S, \text{shape}(I)) \quad (15)$$

3) Superpixel Evaluation: For each superpixel s_i , we calculate the ratio of the intersection between the resized binary mask and the superpixel:

$$R_i = \frac{\sum_{p \in s_i} S_{\text{resized}}(p)}{|s_i|} \quad (16)$$

where $|s_i|$ is the number of pixels in superpixel s_i , and p represents each pixel.

4) Selecting the Best Superpixel: The superpixel with the highest ratio R_i is selected as the best superpixel:

$$s_{\text{best}} = \arg \max R_i \quad (17)$$

I. Lesion's Location

The segmented image is constructed by setting pixels in the best superpixel to 1 and the rest to 0:

$$I_{\text{segmented}}(p) = \begin{cases} 1 & \text{if } p \in s_{\text{best}} \\ 0 & \text{otherwise} \end{cases} \quad (18)$$

This process ensures that the region with the highest probability from the U-Net segmentation aligns with the superpixel boundaries.

1) Prediction Using the Hybrid Model: With all the necessary information provided, the traditional model (SLIC) is now capable of generating a new mask for the (I_{th}) image in the dataset. This paper utilized the small-size mask produced by the U-Net (128x128 pixels) to segment the full-size image. The accuracy of the full-size image segmented by the U-Net can then be compared to that of the Hybrid Model. Due to hardware limitations, particularly with the GPU, the study could not evaluate the U-Net results on the full-size images. However, it was able to process 1024x1024 resized images. Consequently, the Hybrid Model was also applied to these 1024x1024 images to enable a direct comparison of the outputs. Figure 2 shows an example output of the Hybrid Model. The Hybrid Model was also applied to 3900*3900 (full-size) test images to showcase the power of the proposed model.

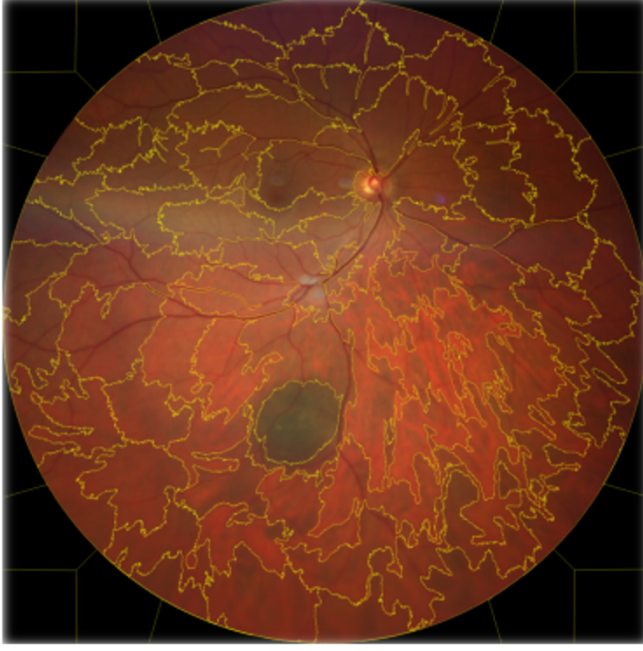


Fig. 2: Eye fundus image, segmented with proposed method

J. Measurements

In segmentation, unlike classification, different metrics are used to assess effectiveness. For a 64x64 pixel image, classification gives a binary output (true or false) per class, easily compared to the ground truth. In segmentation, 4,096 outputs (each pixel) are classified as true or false. Metrics like Intersection Over Union (IoU) and Dice Coefficient evaluate accuracy by comparing the model's output with the ground truth on a pixel level, measuring similarity.

Intersection Over Union: IoU, or the Jaccard Index, was developed by Grove Karl Gilbert in 1884. The Jaccard similarity is determined by dividing the total number of observations in both sets by the total number of observations in either set.

$$J(A, B) = \frac{|A \cap B|}{|A \cup B|} \quad (19)$$

Dice Coefficient: The Sorenson-Dice index, or just the Dice coefficient, is another name for the Dice similarity coefficient, a statistical tool used to compare two data sets. This index has perhaps become the most widely used tool for testing AI-created image segmentation algorithms.

$$Dice(A, B) = \frac{2 \cdot |A \cap B|}{|A| + |B|} \quad (20)$$

K. Hyper-parameter Tuning:

The research utilized Grid Search for hyper-parameter tuning to enhance model performance. Adjustments included varying the learning rate from 0.01 to 0.000001 (decreasing by 10), testing batch sizes of 2, 4, 8, and 16, and evaluating two loss functions: Focal and Dice Loss. This systematic approach helped identify the optimal parameter combination for the models.

VI. RESULTS AND DISCUSSION

The results are produced using two different approaches: the first employed the U-Net method, widely recognized as one of the most effective techniques for medical image segmentation, and the second utilized the Hybrid method. The experiments were designed to ensure that all other factors were kept identical, allowing for a clear and direct comparison between the tested models, thereby highlighting the differences in their performance.

A. First Experiment: U-Net [16] Performance Evaluation

In the first experiment, datasets of varying image sizes were selected to evaluate the performance of the Attention U-Net in terms of segmentation accuracy, time, and energy consumption. The data seed and partitioning ratio were identical across all experiments to ensure consistency and reliability. The training was conducted on a V100 Nvidia GPU provided by the University of Calgary's Advanced Research Computing (ARC) facility. The image sizes used in this experiment were 128x128, 256x256, 512x512, and 1024x1024 pixels. The best performance was observed with 128x128 images, achieving an Intersection over Union (IoU) of 74.82% and a Dice coefficient of 84.32%. In contrast, the worst performance was noted with 1024x1024 images, with an IoU of 34.20% and a Dice coefficient of 51.30%. **Fig5** demonstrates a clear trend: as image size decreases, segmentation accuracy improves. Additionally, as expected, the graph also highlights the significant increase in time and energy consumption when training on larger images. In Fig. 3, the left column represents the prediction accuracy of the test model (measured in percentage), while the right column illustrates the energy usage (depicted by the blue line) and time consumption (depicted by the green line).

B. Second Experiment: Hybrid Model Performance Evaluation

The pre-trained U-Net model for 1024x1024 images was evaluated against the proposed Hybrid Model in the second experiment. The U-Net model produced the same results as in the previous experiment, with an IoU of 34.2% and a Dice coefficient of 51.3%, as the data seed and train/validation/test split were kept consistent. In contrast, the Hybrid Model achieved significantly better performance, with an IoU of 80.1% and a Dice coefficient of 89.7%.

C. Results:

The results, presented in Table IV& V, demonstrate superior accuracy and improved energy and time efficiency compared to the Attention U-Net model. A key advantage of the proposed model is its ability to segment full-size images, a significant challenge for U-Net models that typically require advanced and costly GPU hardware for training. Additionally, while U-Net models rely on GPUs for fast predictions, the proposed model operates efficiently on a standard CPU, making it more accessible for real-world applications. This is particularly important for use cases like fundus image prediction, where models are often deployed on embedded systems, such as



Fig. 3: Accuracy, Energy usage and Time consumption of U-net model with different image sizes

fundus cameras, which typically lack dedicated GPUs. By reducing hardware dependencies, the proposed model offers a more practical solution for large-scale image segmentation in resource-constrained environments without sacrificing performance.

The proposed model outperformed the Attention U-Net model in most of the 24 test images, achieving higher accuracy, as shown in Fig. 4. One of the key strengths of the proposed model is its improved ability to detect the precise edges of lesions, a task where the U-Net model struggled. This enhanced edge detection contributes significantly to the overall accuracy of the segmentation, further demonstrating the advantages of the proposed approach.

D. Segmentation Performance by Quality Groups

To further evaluate the segmentation model's performance, the test set consisting of 25 fundus images was stratified into three groups based on the Dice coefficient:

1) *Good-Performance (Dice ≥ 0.8)*: The **Good-Performance** group consisted of 21 samples, achieving a mean Dice of 0.935 with a 95% CI of [0.914, 0.955]. The sample is shown in Fig. 4. The model architecture proved more effective in these cases, as it was able to enhance the edge details of the lesions more accurately than the U-Net model. Additionally, most images in this group had relatively higher resolution compared to the other two groups. Since the

Models	Measurements	Image Size: 1024*1024	Image Size: 3900*3900
U-Net	IOU	34.20%	N.A
	Dice	51.30%	N.A
	Train Time	129.3 Minutes	N.A
	Device	GPU V100	N.A
	Energy Usage	646.5 Wh	N.A
Hybrid Model	IOU	80.10%	79.60%
	Dice	89.70%	88.20%
	Train Time	3.16 Minutes	3.16 Minutes
	Device	GPU V100	GPU V100
	Energy Usage	15.8 Wh	15.8 Wh

TABLE IV: Comparison of U-Net and Hybrid Model performance on different image sizes.

U-Net component produced segmentations with acceptable error, the second stage, responsible for calculating parameters such as approximate lesion diameter, lesion location, and pixel-wise probability, was able to perform with minimal error, contributing to the strong segmentation performance of the SLIC component.

2) *Moderate-Performance (0.5 \leq Dice < 0.8)*: The **Moderate-Performance** group comprised 2 samples with a mean Dice of 0.618 (95% CI: [0.308, 0.929]). Although the overall image quality is good in these two images, the lesion blends into the background, making it difficult for the Hybrid model to segment it accurately. This challenge is particularly evident in the lightweight U-Net component, which tends to under-perform in regions where lesion boundaries are poorly defined. While the SLIC component generally handles such cases better due to its colour-based clustering, its performance is hindered when the U-Net provides inaccurate initial approximations of the lesion size, leading to unreliable inputs for the SLIC stage. Simultaneously, the large-scale U-Net model (1024×1024) demonstrated improved performance, highlighting the importance of higher-resolution images in cases where the lesion is not clearly distinguishable from the background and appears to blend into it (Fig. 5).

3) *Poor-Performance (Dice < 0.5)*: The **Poor-Performance** group included 2 samples with a mean Dice of 0.129 and a 95% confidence interval (CI) of [-1.511, 1.769]. In this group, poor performance can be attributed to several factors. The lesions were notably smaller, often faded into the background, and the image quality was generally lower compared to the rest of the test dataset. Since machine learning models like U-Net are sensitive to the signal-to-noise ratio, a smaller lesion area relative to the background increases this ratio, resulting in higher segmentation errors. This effect, combined with the

Models	Measurements	Image Size: 1024×1024
U-Net	Hausdorff Distance	77.91 px
	Precision	46.41%
	Sensitivity (Recall)	81.84%
	Specificity	98.77%
	Volumetric Similarity	72.37%
Hybrid Model (Math Method)	Hausdorff Distance	21.6 px
	Precision	93.45%
	Sensitivity (Recall)	85.10%
	Specificity	99.92%
	Volumetric Similarity	95.32%

TABLE V: Performance comparison between U-Net and Hybrid Model on 1024×1024 fundus images.

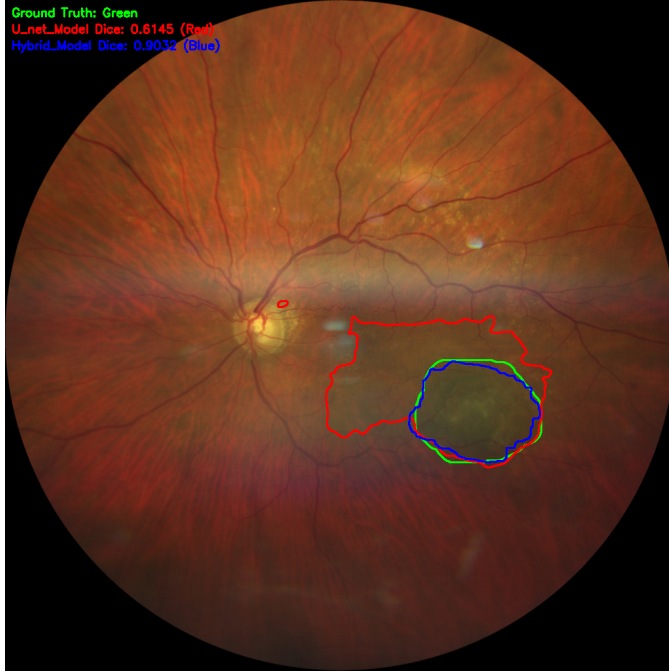


Fig. 4: Sample where proposed model performs well

fading lesions observed in the Moderate-Performance group and the increased noise from image blurriness, substantially reduces the accuracy of the lightweight U-Net (128×128) component in the Hybrid model, leading to less reliable inputs for the SLIC stage. Furthermore, as illustrated in Fig. 6, the large-scale U-Net model (1024×1024) also exhibits significant errors, underscoring U-Net's vulnerability to noisy imaging conditions.

4) *Kruskal–Wallis test*: Also the Kruskal–Wallis test was conducted to assess statistical differences among the groups, revealing a significant difference in Dice scores ($P = 0.0076$). This suggests that the grouping reflects meaningful distinctions

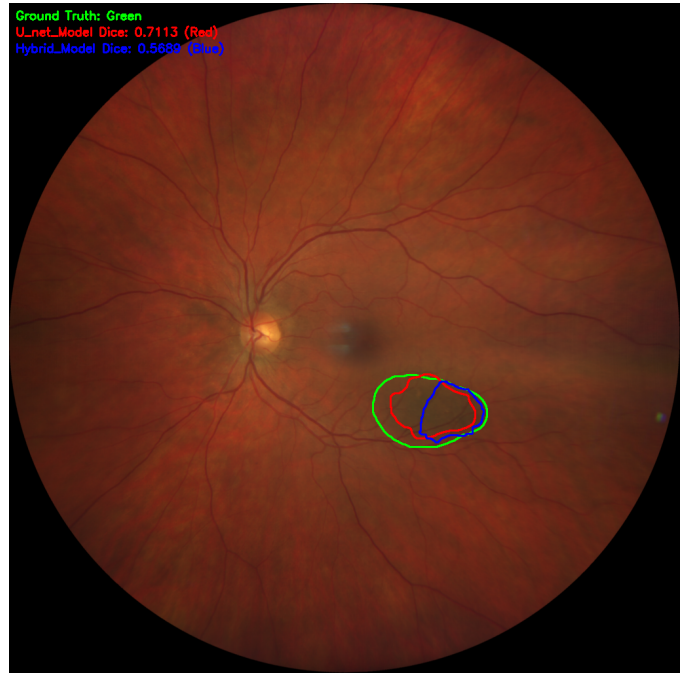


Fig. 5: Sample where proposed model performs moderately

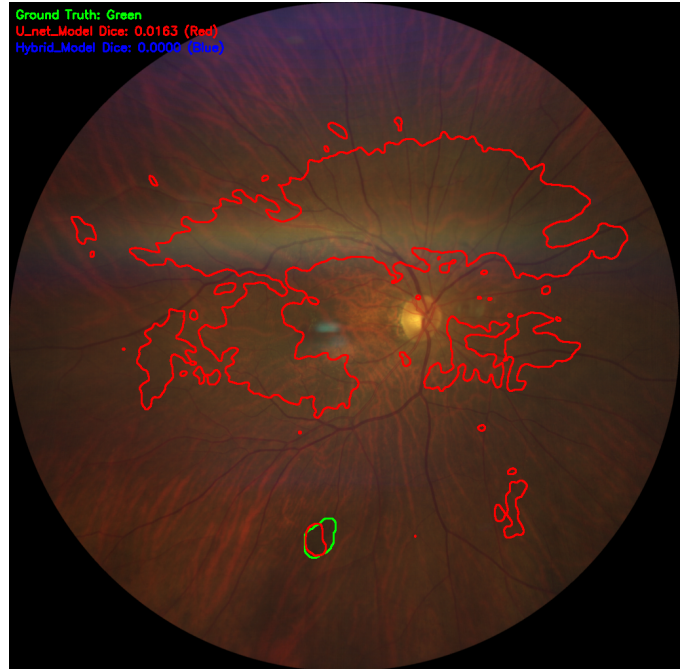


Fig. 6: Sample where proposed model performs weakly

in segmentation quality across the test samples.

5) *Limitations*: A notable limitation of the proposed model arises from its reliance on a small-size U-Net (128x128) for parameter calculation. If the U-Net fails to identify any meaningful features in the input image, the proposed model will likely fail. This dependency occurs because the proposed model relies on the information generated by the small-size U-Net to compute its parameters. When the U-Net does not provide sufficient data, the proposed model lacks the raw input necessary for accurate prediction. Fig 6 illustrates examples of

such cases.

6) The Proposed Method Performance: In several instances, the proposed model performed better than expected. It is important first to acknowledge the limitations inherent in the masks created by specialists, which may contain minor inaccuracies due to factors such as colour degradation at the edges or the smoothing of small rough edges to save time. Despite these challenges, the model could precisely capture the shape of lesions with irregular, dented edges, even without similar patterns in the training data. The right image in Fig 7 illustrates this capability. Another area where the model excelled is handling images with significant noise, which typically confuses U-Net-based models. Despite the noise, the proposed model could accurately capture the lesion shape in such cases. The left image in Fig 7 demonstrates a noisy image where the model successfully overcame the noise and precisely identified the lesion area. This robust performance makes the model more reliable for real-world applications, particularly in cases where precise lesion measurement is essential for tracking growth over time.

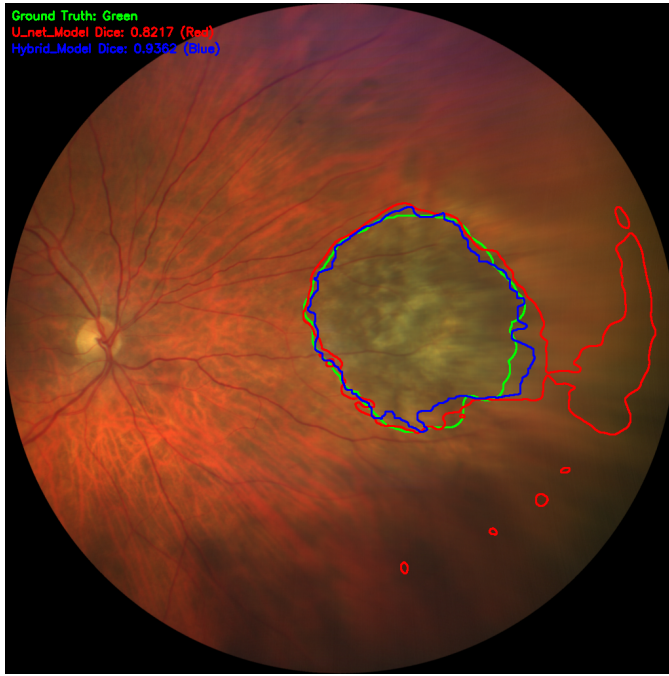


Fig. 7: Sample where proposed model performs better than expected

E. Generalizability of the Results

An external dataset from Wills Eye Hospital was used to evaluate the model's generalizability across different fundus cameras and domains. The results indicate a significant drop in accuracy for the U-Net model when applied to various domains, as shown in Table VI. In contrast, the proposed architecture demonstrates improved accuracy under domain shifts, indicating greater robustness in handling domain variations in image segmentation tasks, as shown in Table VII. Nonetheless, performance could potentially be enhanced by incorporating Domain Adaptation techniques to address the domain shift

challenge in U-Net. This would enable U-Net to provide more accurate parameters for the SLIC model, further improving segmentation outcomes.

Prediction	Measurement	Image Size	
		1024	128
U-net Results	IOU	37.05%	55.01%
	Dice	54.06%	73.02%

TABLE VI: Wills Eye Hospital dataset, predicted using trained model

Prediction	Measurement	Image Size	
		1024	128
U-net Results	IOU	37.05%	55.01%
	Dice	54.06%	73.02%
Hybrid Model	IOU	59.20%	
	Dice	76.70%	

TABLE VII: Wills Eye Hospital dataset, predicted using proposed model

F. Sensitivity Analysis

Sensitivity analysis assesses the impact of key input parameters on the model's predictions. This analysis is essential for understanding how variability in the model's inputs influences the output, thereby identifying the most influential parameters and ensuring the robustness of the predictions. The paper employed a grid search function to determine the optimal range for the sigma parameter, systematically exploring the parameter space to find the best possible setting for maximizing model performance.

Sigma: This parameter defines the standard deviation of the Gaussian kernel applied to the input image in the SLIC function. Sigma is crucial in smoothing the image and controlling sensitivity to noise and small details. In larger images, adjusting sigma can help better capture meaningful features while reducing the impact of noise. The best results are observed when the sigma parameter was set between 1.5 and 2. However, higher values may benefit larger images by balancing the trade-off between fine details and noise reduction.

G. Computational Efficiency:

Referring to Table IV, the proposed Hybrid Model demonstrates significantly higher computational efficiency, as it eliminates the need for GPU acceleration even when processing full-size images (3900×3900 pixels). This feature makes the model well-suited for integration into clinical devices without requiring hardware upgrades. For several reasons, embedding the algorithm directly within a fundoscopy camera would be

highly advantageous. First, since fundus images are as unique as fingerprints, transmitting them over the internet introduces considerable challenges related to data security and patient privacy. Second, local deployment ensures more reliable access to the software, especially in settings where internet connectivity may be intermittent. The low computational cost of the Hybrid Model thus facilitates its implementation directly within the camera hardware, making it a practical and secure solution for clinical use.

H. Discussion (Clinical Perspective):

This study offers clinically meaningful improvements in lesion segmentation, enabling more accurate identification of choroidal nevi in fundus images. This can support clinicians in monitoring lesion stability over time and detecting early signs of growth. By improving segmentation precision, the model helps identify lesions at risk of malignant transformation, allowing for earlier referral and intervention. Its efficiency and ability to run on standard hardware make it suitable for real-world clinical use.

VII. CONCLUSION

This paper presents a novel approach for segmenting CN lesions in fundus images, addressing the key challenges posed by indistinct lesion boundaries and fading colour spectra by integrating CNN models with traditional segmentation methods for automated fundus image segmentation. This method demonstrates improved accuracy in CN lesion detection. This advancement can enhance the generalizability of predictive models while reducing the computational and environmental costs associated with their training and deployment. Ultimately, the methods introduced in this research represents a significant step forward in the precise and reliable segmentation of CN lesions. It is critical for early detection and better clinical outcomes in diagnosing and managing CN.

VIII. FUTURE WORK

Future work in this lab will focus on developing and refining image segmentation techniques using mathematical approaches to increase the accuracy of image segmentation in medical images. This strategy aims to enhance segmentation accuracy while minimizing dependency on large datasets.

A. Lesion Growth Tracking

This direction will establish a foundation for robust methods to track lesion growth over time. Accurate monitoring of lesion progression and associated risk factors can equip specialists with more effective tools for assessing the risk of ocular diseases. Ultimately, this advancement is intended to streamline diagnostic workflows and improve patient outcomes through more comprehensive and timely evaluations of ocular health.

B. U-Net Dependency

As highlighted in our previous research [13], employing an ensemble of U-Net models can significantly boost segmentation accuracy. This enhancement has the potential to improve the overall performance of the Hybrid Model, combining the strengths of both deep learning and analytical methods.

C. Loss Function Improvement

We are currently investigating the integration of the SLIC model into the loss function of the U-Net architecture. This research explores the possibility of embedding the benefits of the Hybrid method directly into the learning process, potentially enhancing the model's performance through a more informed optimization objective.

REFERENCES

- [1] Yaroub Elloumi, Mohamed Akil, and Henda Boudeggaa. Ocular diseases diagnosis in fundus images using a deep learning: approaches, tools and performance evaluation. In *Real-Time Image Processing and Deep Learning 2019*, volume 10996, pages 221–228. SPIE, 2019.
- [2] R Trafford Crump, Emad Mohammed, Mehregan Biglarbeiki, Mohammad Mahdi Eshragh, Esmail Shakeri, Gunnar Joakin Siljedal, Behrouz Far, and Ezekiel Weis. Artificial intelligence in the classification and segmentation of fundus images with choroidal nevi. *Canadian Journal of Ophthalmology*, 2024. Publisher: Elsevier.
- [3] Sharon H. Saydah, Robert B. Gerzoff, Jinan B. Saaddine, Xinzhi Zhang, and Mary Frances Cotch. Eye Care Among US Adults at High Risk for Vision Loss in the United States in 2002 and 2017. *JAMA Ophthalmology*, 138(5):479, May 2020.
- [4] Salvador Gomez, Maura Di Nicola, Nathan L. Scott, and Basil K. Williams. Health disparities in ocular oncology. *Canadian Journal of Ophthalmology*, 59(6):369–375, December 2024.
- [5] Patrick J. Saine and Marshall E. Tyler. *Ophthalmic photography: retinal photography, angiography, and electronic imaging*. Butterworth-Heinemann, Boston, 2nd ed edition, 2002.
- [6] A Schalénbourg and L Zografos. Pitfalls in colour photography of choroidal tumours. *Eye*, 27(2):224–229, 2013. Publisher: Nature Publishing Group.
- [7] Albert Cheung, I Scott, T Murray, and CL Shields. Distinguishing a choroidal nevus from a choroidal melanoma. *EyeNet Mag*, pages 39–40, 2012.
- [8] Esmail Shakeri, Trafford Crump, Ezekiel Weis, Emad Mohammed, Roberto Souza, and Behrouz Far. Explaining eye diseases detected by machine learning using shap: A case study of diabetic retinopathy and choroidal nevus. *SN Computer Science*, 4(5):433, 2023. Publisher: Springer.
- [9] Esmail Shakeri, Emad Mohammed, Trafford Crump, Ezekiel Weis, Carol L Shields, Sandor R Ferenczy, and Behrouz Far. Deep Learning-Based Detection and Classification of Uveal Melanoma Using Convolutional Neural Networks and SHAP Analysis. In *2023 IEEE 24th International Conference on Information Reuse and Integration for Data Science (IRI)*, pages 215–220. IEEE, 2023.
- [10] Esmail Shakeri, Emad A Mohammed, Zahra Shakeri HA, and Behrouz Far. Exploring features contributing to the early prediction of sepsis using machine learning. In *2021 43rd Annual International Conference of the IEEE Engineering in Medicine & Biology Society (EMBC)*, pages 2472–2475. IEEE, 2021.
- [11] Mehregan Biglarbeiki, Emad Mohammed, Roberto Souza, Behrouz Far, Ezekiel Weis, and Trafford Crump. Choroidal Nevi Classification in Fundus Images Using a Patch-Based Deep Learning Approach. In *2023 IEEE EMBS Special Topic Conference on Data Science and Engineering in Healthcare, Medicine and Biology*, pages 177–178, Malta, December 2023. IEEE.
- [12] Mehregan Biglarbeiki, Ezekiel Weis, Emad Mohammed, Roberto Souza, Behrouz Far, and Trafford Crump. Automated Classification of Choroidal Nevi using Data Augmentation and a Patch-Based Deep Learning Approach with Fundus Images. *Investigative Ophthalmology & Visual Science*, 65(7):OD57–OD57, 2024. Publisher: The Association for Research in Vision and Ophthalmology.

[13] Mohammadmahdi Eshragh, Emad A. Mohammed, Behrouz Far, Trafford Crump, and Ezekiel Weis. Enhancing Choroidal Nevus Position Identification through CNN-Based Segmentation of Eye Fundus Images. In *2024 46th Annual International Conference of the IEEE Engineering in Medicine and Biology Society (EMBC)*, pages 1–4, Orlando, FL, USA, July 2024. IEEE.

[14] Tomasz Krzywicki, Piotr Brona, Agnieszka M. Zbrzezny, and Andrzej E. Grzybowski. A Global Review of Publicly Available Datasets Containing Fundus Images: Characteristics, Barriers to Access, Usability, and Generalizability. *Journal of Clinical Medicine*, 12(10):3587, May 2023.

[15] Simon Jégou, Michał Drozdzał, David Vazquez, Adriana Romero, and Yoshua Bengio. The one hundred layers *tiramisu*: Fully convolutional densenets for semantic segmentation. In *Proceedings of the IEEE conference on computer vision and pattern recognition workshops*, pages 11–19, 2017.

[16] Olaf Ronneberger, Philipp Fischer, and Thomas Brox. U-net: Convolutional networks for biomedical image segmentation. In *Medical image computing and computer-assisted intervention–MICCAI 2015: 18th international conference, Munich, Germany, October 5–9, 2015, proceedings, part III 18*, pages 234–241. Springer, 2015.

[17] Md Zahangir Alom, Chris Yakopcic, Mahmudul Hasan, Tarek M Taha, and Vijayan K Asari. Recurrent residual U-Net for medical image segmentation. *Journal of medical imaging*, 6(1):014006–014006, 2019. Publisher: Society of Photo-Optical Instrumentation Engineers.

[18] Md Zahangir Alom, Mahmudul Hasan, Chris Yakopcic, Tarek M Taha, and Vijayan K Asari. Recurrent residual convolutional neural network based on u-net (r2u-net) for medical image segmentation. *arXiv preprint arXiv:1802.06955*, 2018.

[19] Wenjun Yan, Yuan Yuan Wang, Shengjia Gu, Lu Huang, Fuhua Yan, Liming Xia, and Qian Tao. The domain shift problem of medical image segmentation and vendor-adaptation by Unet-GAN. In *Medical Image Computing and Computer Assisted Intervention–MICCAI 2019: 22nd International Conference, Shenzhen, China, October 13–17, 2019, Proceedings, Part II 22*, pages 623–631. Springer, 2019.

[20] Peer Neubert and Peter Protzel. Compact watershed and preemptive slic: On improving trade-offs of superpixel segmentation algorithms. In *2014 22nd international conference on pattern recognition*, pages 996–1001. IEEE, 2014.

[21] Pedro F Felzenszwalb and Daniel P Huttenlocher. Efficient graph-based image segmentation. *International journal of computer vision*, 59:167–181, 2004. Publisher: Springer.

[22] Radhakrishna Achanta, Appu Shaji, Kevin Smith, Aurelien Lucchi, Pascal Fua, and Sabine Süsstrunk. SLIC superpixels compared to state-of-the-art superpixel methods. *IEEE transactions on pattern analysis and machine intelligence*, 34(11):2274–2282, 2012. Publisher: IEEE.

[23] Yun Jiang, Falin Wang, Jing Gao, and Simin Cao. Multi-path recurrent U-Net segmentation of retinal fundus image. *Applied Sciences*, 10(11):3777, 2020. Publisher: MDPI.

[24] Jayanthi Sivaswamy, S. R. Krishnadas, Gopal Datt Joshi, Madhulika Jain, and A. Ujjwaal Syed Tabish. Drishti-GS: Retinal image dataset for optic nerve head(ONH) segmentation. In *2014 IEEE 11th International Symposium on Biomedical Imaging (ISBI)*, pages 53–56, Beijing, China, April 2014. IEEE.

[25] Xiaoye Zhao, Shengying Wang, Jing Zhao, Haicheng Wei, Mingxia Xiao, and Na Ta. Application of an attention u-net incorporating transfer learning for optic disc and cup segmentation. *Signal, Image and Video Processing*, 15:913–921, 2021. Publisher: Springer.

[26] AS Shirokanov, N Yu Ilyasova, and NS Demin. Analysis of convolutional neural network for fundus image segmentation. In *Journal of Physics: Conference Series*, volume 1438, page 012016. IOP Publishing, 2020. Issue: 1.

[27] Zan Li, Hong Zhang, Zhengzhen Li, and Zuyue Ren. Residual-attention unet++: a nested residual-attention u-net for medical image segmentation. *Applied Sciences*, 12(14):7149, 2022. Publisher: MDPI.

[28] Mehreen Mubashar, Hazrat Ali, Christer Grönlund, and Shoaib Azmat. R2U++: a multiscale recurrent residual U-Net with dense skip connections for medical image segmentation. *Neural Computing and Applications*, 34(20):17723–17739, 2022. Publisher: Springer.

[29] Mehregan Biglarbeiki, Roberto Souza, Emad Mohammed, Ezekiel Weis, Carol L. Shields, Sandor R. Ferenczy, Behrouz Far, and Trafford Crump. Enhancing Choroidal Nevus Segmentation in Fundus Images Using YOLO. In *2024 IEEE International Conference on Information Reuse and Integration for Data Science (IRI)*, pages 102–107, San Jose, CA, USA, August 2024. IEEE.

[30] Meindert Niemeijer, Michael D. Abràmoff, and Bram Van Ginneken. Publicly available retinal image data and the use of competitions to standardize algorithm performance comparison. In Ratko Magajevic, Olaf Dössel, and Wolfgang C. Schlegel, editors, *World Congress on Medical Physics and Biomedical Engineering, September 7 - 12, 2009, Munich, Germany*, volume 25/11, pages 175–178. Springer Berlin Heidelberg, Berlin, Heidelberg, 2009. Series Title: IFMBE Proceedings.

[31] John Lafferty, Andrew McCallum, Fernando Pereira, and others. Conditional random fields: Probabilistic models for segmenting and labeling sequence data. In *Icml*, volume 1, page 3. Williamstown, MA, 2001. Issue: 2.

[32] Andrea Vedaldi and Stefano Soatto. Quick shift and kernel methods for mode seeking. In *Computer Vision–ECCV 2008: 10th European Conference on Computer Vision, Marseille, France, October 12–18, 2008, Proceedings, Part IV 10*, pages 705–718. Springer, 2008.

[33] Ozan Oktay, Jo Schlemper, Loïc Le Folgoc, Matthew Lee, Matthias Heinrich, Kazunari Misawa, Kensaku Mori, Steven McDonagh, Nils Y Hammerla, Bernhard Kainz, and others. Attention u-net: Learning where to look for the pancreas. *arXiv preprint arXiv:1804.03999*, 2018.